Available online at www.sciencedirect.com
ScienceDirect
Journal of Solid State Chemistry 180 (2007) 2603–2615
JOURNAL OF SOLID STATE CHEMISTRY
www.elsevier.com/locate/jssc

Effect of metal doping on the low-temperature structural behavior of thermoelectric β-Zn_4Sb_3

Johanna Nylén[a], Sven Lidin[a], Magnus Andersson[b], Hongxue Liu[c], Nate Newman[c], Ulrich Häussermann[d,*]

[a]*Inorganic Chemistry, Stockholm University, SE-10691 Stockholm, Sweden*
[b]*Solid State Physics, IMIT, Royal Institute of Technology, KTH Electrum 229, SE-16440 Kista, Sweden*
[c]*School of Materials, Arizona State University, P.O. Box 876006, Tempe, AZ 85287-6006, USA*
[d]*Department of Chemistry and Biochemistry, Arizona State University, P.O. Box 871604, Tempe, AZ 85287-1604, USA*

Received 13 June 2007; received in revised form 13 July 2007; accepted 15 July 2007
Available online 26 July 2007

Abstract

The low-temperature structural phase transitions of Bi, Pb, In and Sn-doped samples of thermoelectric Zn_4Sb_3 have been characterized on crystals grown from molten metal fluxes, using electrical resistance and single crystal X-ray diffraction measurements. Room temperature stable, disordered, β-Zn_4Sb_3 undergoes two phase transitions at 254 and 235 K to the consecutively higher ordered phases α and α', respectively. The ideal crystallographic composition of α-Zn_4Sb_3 is $Zn_{13}Sb_{10}$. The α–α' transformation is triggered by a slight and homogenous Zn deficiency with respect to this composition and introduces a compositional modulation in the α-Zn_4Sb_3 structure. When preparing β-Zn_4Sb_3 in the presence of metals with low melting points (Bi, Sn, In, Pb) the additional metal atoms are unavoidably incorporated in small concentrations (0.04–1.3 at%) and act as dopants. This incorporation alters the subtle balance between Zn disorder and Zn deficiency in Zn_4Sb_3 and has dramatic consequences for its low-temperature structural behavior. From molten metal flux synthesis it is possible to obtain (doped) Zn_4Sb_3 samples which (1) only display a β–α transition, (2) only display a β–α' transition, or (3) do not display any low-temperature phase transition at all. Case (2) provided diffraction data with a sufficient quality to obtain a structural model for highly complex, compositionally modulated, α'-Zn_4Sb_3. The crystallographic composition of this phase is $Zn_{84}Sb_{65}$.

Keywords: Temperature polymorphism; Thermoelectric materials; Zinc antimonides; Order–disorder structural transitions

1. Introduction

Power-generating devices based on thermoelectric technology can play an important role in satisfying the future global need for efficient energy management [1]. However, the development of thermoelectric materials has proven to be a difficult and frustrating journey with slow progress [2–4]. A good thermoelectric material is characterized by a high thermopower S combined with a low electrical resistivity ρ and a low thermal conductivity κ [4–6] The latter is a sum of an electronic and a lattice contribution, κ_e and κ_L, respectively. Because the set of properties arise from common physical origins they are interdependent and cannot be optimized separately. Usually good thermoelectrics are narrow gap semiconductors, which have to be heavily doped [7]. The latter step adjusts the carrier concentration toward an optimum power factor, S^2/ρ. In addition, the material must have values of the thermal conductivity that approach those of poorly conducting amorphous materials.

The possibilities to reduce κ_L are very much linked to the crystal chemistry of a particular material [4–6]. Low thermal conductivity can be expected in compounds with a large average mass of its constituent atoms and/or in compounds with complex, large unit cell structures. Further, κ_L can be decreased by alloying or by the presence of loosely bonded atoms (rattlers) in the crystal structure. However, a most effective means to low values of κ_L is structural disorder beyond alloying because it can provide

*Corresponding author. Fax: +1 480 965 2747.
E-mail address: Ulrich.Haussermann@asu.edu (U. Häussermann).

0022-4596/$ - see front matter © 2007 Elsevier Inc. All rights reserved.
doi:10.1016/j.jssc.2007.07.013

additional scattering mechanisms that also affect mid and long-wave-length phonons [8,9]. The challenge with structurally disordered systems is the difficulty to control their composition and the resulting electronic properties important for thermoelectric performance.

β-Zn_4Sb_3 is a structurally disordered narrow-gap semiconductor which has recently emerged as a prospective *p*-type thermoelectric for the moderate temperature range (450–650 K), mainly because of its exceptional low thermal conductivity (0.9 W/Km at room temperature) [10]. The disorder is expressed as a combination of defects and interstitial Zn atoms and results in a crystallographically variable Zn composition [11,12]. Furthermore, Zn disorder in β-Zn_4Sb_3 gives rise to polymorphism at low temperatures where increasingly complex and more ordered structures are formed [13,14]. Although the low-temperature polymorphism of Zn_4Sb_3 is complicated to analyze it provides at the same time a key for a better understanding of the intricate composition–property relations of this material. In this work we describe how the incorporation of small amounts of an additional metal (around 1 at%) in Zn_4Sb_3 radically changes its low-temperature structural behavior by influencing the delicately balanced Zn disorder. Moreover, metal doping of Zn_4Sb_3 slightly but decisively alters the Zn/Sb ratio of the bulk material. This has consequences for the electronic properties of the material and offers opportunities for optimizing its thermoelectric performance.

The paper is organized as follows: In Section 2 we review the structural and thermoelectric properties of Zn_4Sb_3. Importantly, we attempt to give new structure/composition insights in order to interpret ambiguous results reported in the literature over the past decade. In Section 3 we describe our synthesis method for metal-doped Zn_4Sb_3 samples, Sections 4 and 5 are devoted to the electrical resistivity and structural properties of doped Zn_4Sb_3, respectively, at low temperatures.

2. Structural and thermoelectric properties of Zn_4Sb_3

Although Zn_4Sb_3 was discovered and studied in detail already in the late 1960s [15,16], its good thermoelectric performance was recognized only recently in the course of a careful reinvestigation of its transport properties [10]. The key to the high thermoelectric performance lies in the exceptionally low thermal conductivity. Zn_4Sb_3 displays intricate temperature polymorphism. Room temperature stable β-Zn_4Sb_3 transforms at about 765 K into a high-temperature γ modification [17,18]. At even higher temperatures two more modifications (δ and δ') have been proposed [18]. The composition interval presumably shifts to lower Zn contents above the β–γ transition. At 841 K Zn_4Sb_3 melts congruently. At low temperatures β-Zn_4Sb_3 undergoes a phase transition to α-Zn_4Sb_3 (254 K) [13]. Below 235 K a second low-temperature phase (α'-Zn_4Sb_3) can be detected [14,19]. Zn_4Sb_3 possesses a small homogeneity interval (<1 at%), at least for temperatures below 673 K [18,20].

The room temperature thermoelectric properties for β-Zn_4Sb_3 according to Ref. [10] are $S = 113\,\mu V/K$, $\rho = 2\,m\Omega\,cm$, $\kappa = 9\,mW/(cm\,K)$ and carrier concentration $p = 9 \times 10^{19}\,cm^{-3}$. The thermoelectric figure of merit $ZT = S^2/(\rho\kappa)T$ rises from about 0.2 at room temperature to a maximum value of 1.3 at 650 K, after which it degrades rapidly. This degradation is probably connected with the β–γ phase transition and/or an impoverishment of Zn.

The structure of room temperature β-Zn_4Sb_3 was originally solved and refined from single crystal X-ray data by Mayer et al. in 1978 [21]. According to the obtained model, β-Zn_4Sb_3 is rhombohedral (space group $R\bar{3}c$) with 66 atoms (36 Zn and 30 Sb) in the hexagonal unit cell. This yields a crystallographic composition Zn_6Sb_5 (54.5 at% Zn). In their refinement Mayer at al. introduced a Zn/Sb mixed occupied position in order to account for the considerable deviation from the nominal synthesis composition Zn_4Sb_3 (57.1 at% Zn). A recent reinvestigation of the β-Zn_4Sb_3 structure by Mozharivskyj et al. [17] questioned this mixed occupied position. Instead, these authors found considerable occupational deficiency on the Zn atomic position and suggested to describe β-Zn_4Sb_3 as $Zn_{6-\delta}Sb_5$ with δ varying between 0.6 and 0.4. This, however, puts the crystallographic Zn content as low as 51.8–53.3 at%. Finally, Snyder et al. [11] and Cargnoni et al. [12] presented a completely new view on the β-Zn_4Sb_3 structure. Small regions of extra electron density were identified and subsequently refined as weakly occupied interstitial Zn positions. With these interstitials the crystallographic Zn content of β-Zn_4Sb_3 increased to 56.1 at% (i.e., a composition $Zn_{3.84}Sb_3$) and an ideal stoichiometry $Zn_{13}Sb_{10}$ ($Zn_{3.9}Sb_3$, 56.5 at% Zn) was proposed.

The interstitial Zn atom model for β-Zn_4Sb_3 is appealing: It assures a more Zn-rich composition for Zn_4Sb_3 in better agreement with the nominal composition, and provides a ready explanation for the low thermal conductivity in terms of structural disorder. The crystal structure of a hypothetical disorder-free β-Zn_4Sb_3 (i.e., a framework $Zn_{12}Sb_{10}$) consists of three distinct atomic positions (36*f* Zn, 18*e* Sb1, 12*c* Sb2) and is shown in Fig. 1a. Zn and Sb1 display a peculiar 5- and 6-coordination, respectively, and form planar rhomboid rings, Zn_2Sb1_2 – with a short Zn contact (2.8 Å) – that are further condensed into chains by sharing common Sb1 atoms (Fig. 1b). These chains run in three different directions and are linked by Zn–Sb1 bonds, which results in channels along the *c* direction. In the final framework $Zn_{12}Sb_{10}$ the channels are centered by Sb2 atoms, which attain a tetrahedral 4-coordination by binding to an additional Sb2 atom and to three Zn atoms residing in rhomboid ring chains. Zn disorder in β-Zn_4Sb_3 manifests itself in interstitial Zn atoms distributed on three weakly occupied (to about 6%) general sites 36*f*. Additionally, the regular Zn position displays a considerable occupational deficiency (89–90%) [11,12].

The partly occupied Zn positions (framework vacancies and interstitials) represent an average picture of Zn

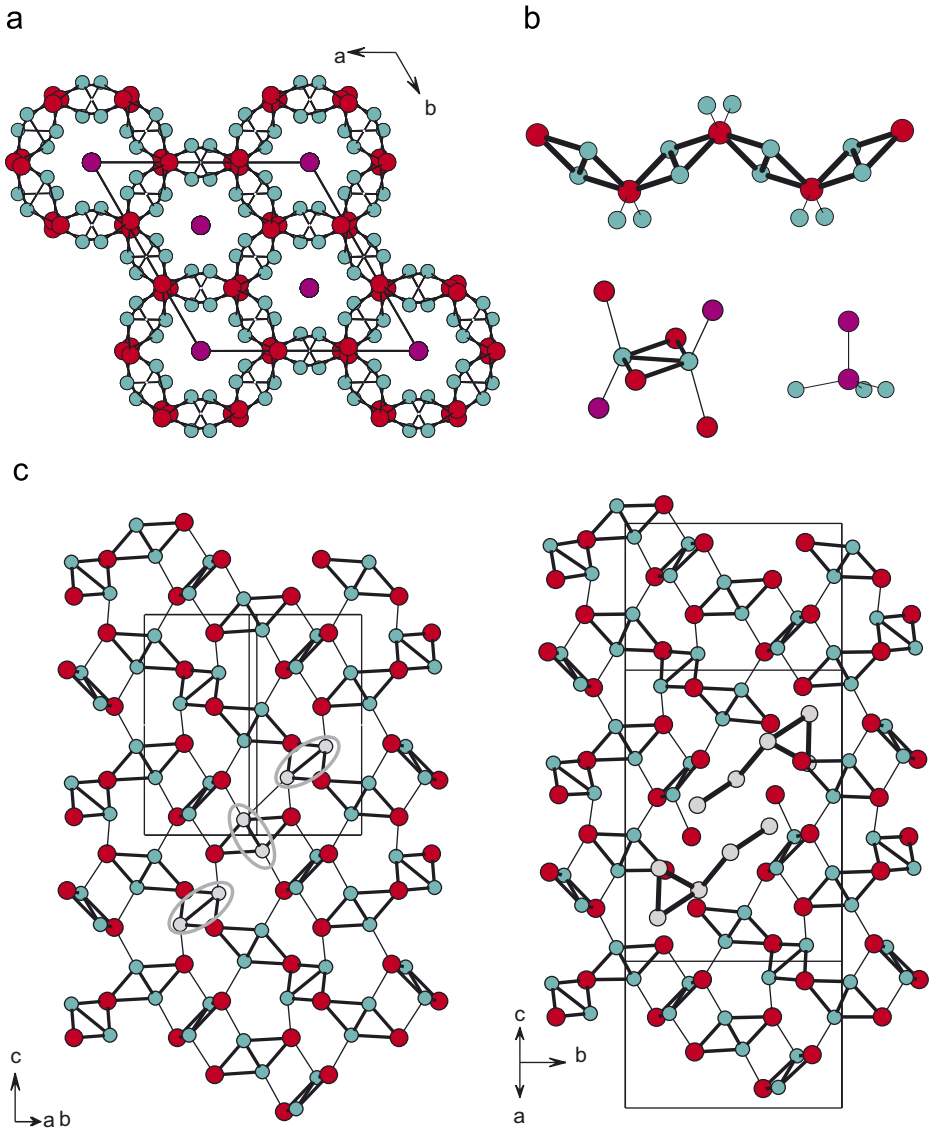

Fig. 1. (a) The rhombohedral $Zn_{12}Sb_{10}$ framework of hypothetical, disorder-free, β-Zn_4Sb_3. Turquoise circles denote Zn atoms, red and purple circles denote the two different types of Sb atoms (Sb1 and Sb2, respectively). The framework is built from chains of condensed rhomboid rings Zn_2Sb1_2 (emphasized with bold lines (cf. Fig. 1b top)) and consists of channels, which are stuffed by Sb2 atoms. (b) Segment of a chain of rhomboid rings Zn_2Sb1_2 in $Zn_{12}Sb_{10}$ (top). Coordination environment for Zn (bottom left) and Sb2 (bottom right). (c) Equivalent sections of the rhombohedral $Zn_{12}Sb_{10}$ framework (left) and the triclinic α-Zn_4Sb_3 structure (right). Sb2 atoms are omitted for clarity. Regular ("rhombohedral") Zn atoms are drawn as turquoise and interstitial Zn atoms (arranged as five-atom clusters) as gray circles. In the section of $Zn_{12}Sb_{10}$ the pairs of regular Zn atoms missing in α-Zn_4Sb_3 are highlighted. Two five-atom clusters of non-rhombohedral Zn atoms ("interstitials") replace three pairs of Zn atoms from the rhombohedral framework ("vacancies"). Note, that in the real β-Zn_4Sb_3 structure vacancies and interstitials occur randomly disordered, but presumably in a correlated manner (e.g., triangles of interstitials replace pairs of regular Zn atoms [12]).

disorder as obtained from X-ray crystallography and cause ambiguity with respect to the precise composition of β-Zn_4Sb_3. A microscopic model of this disorder was proposed by Cargnoni et al. by assuming β-Zn_4Sb_3 being composed as a mixture of three differently filled (rhombohedral) unit cells: (i) disorder free ($Zn(fr)_{12}Sb_{10}$), (ii) one framework Zn atom is replaced by a pair of interstitials ($Zn(fr)_{11}(Zn(i)_2Sb_{10}$) and (iii) a pair of framework Zn atoms is replaced by a triangle of interstitials ($Zn(fr)_{10}Zn(i)_3Sb_{10}$) [12]. Although there is no experimental proof for this model, it appears reasonable when considering the α-Zn_4Sb_3 structure.

At around 254 K Zn disordered β-Zn_4Sb_3 transforms into α-Zn_4Sb_3 where framework and interstitial Zn atoms order into distinct crystallographic sites. (The Sb substructure remains virtually unaffected). The α-Zn_4Sb_3 structure is triclinic with a metrically monoclinic unit cell ($a \approx 32.5$ Å, $b \approx 12.2$ Å, $c \approx 10.9$ Å, $\beta \approx 99°$) [13]. The two Sb positions in β-Zn_4Sb_3 split into 20 independent positions, while Zn occupies 26 independent positions. Twenty one

out of the 26 Zn positions in α-Zn_4Sb_3 correspond to regular framework Zn atoms arranged in pairs within the rhomboid rings in β-Zn_4Sb_3. The remaining five positions are then associated with the interstitial Zn atoms in disordered β-Zn_4Sb_3. These atoms are assembled in clusters consisting of a triangle with a tail of two more Zn atoms. Two five-atom clusters are grouped together and related by a centre of inversion. Each pair of five-atom clusters replaces three pairs of Zn atoms from the regular rhomboid ring framework in β-Zn_4Sb_3 (Fig. 1c) [22]. These missing pairs of Zn atoms are associated with the vacancies in β-Zn_4Sb_3. The relation to the proposed disorder model of β-Zn_4Sb_3 is striking: Randomly distributed triangles and pairs of interstitials replacing pairs and single Zn atoms in the regular framework, respectively, order into arrays where two five-atom clusters of interstitials (consisting of a triangle with a pair attached) group around a cluster of three pairs of defects.

The α–β transition is reversible in single crystal X-ray diffraction experiments [13]. Therefore, the compositions of α- and β-Zn_4Sb_3 should be the same. The ideal (crystallographic) composition of ordered α-Zn_4Sb_3 amounts to $Zn_{13}Sb_{10}$ ($Zn_{3.9}Sb_3$). However, despite of all atoms being located on distinct sites in the α-Zn_4Sb_3 structure, it is difficult to ascertain full occupancy of the Zn positions because of the combination of a high degree of pseudo-symmetry and twinning [19]. For example, the clusters forming interstitial atoms display large thermal displacement parameters indicative of Zn deficiency. The actual composition of Zn_4Sb_3 is rather expressed as $Zn_{13-\delta}Sb_{10}$ ($\delta = 0.2$–0.5). The Zn deficiency δ is probably associated with the *p*-type conductivity of Zn_4Sb_3 and should also relate to its carrier concentration. Moreover, δ is believed to be the driving force behind the second low-temperature transition [14].

At around 235 K α-Zn_4Sb_3 transforms from into α′-Zn_4Sb_3. The formation of α′-Zn_4Sb_3 corresponds to a further step of ordering, now with respect to the Zn deficiency δ. This is best visualized when viewing the β and α structures along [0 1 0] (Fig. 2). The rhombohedral structure of β-Zn_4Sb_3 can be seen to consist of a number of fine lamellae of identical constitution, repeating along the (hexagonal) [1 0 $\bar{1}$] direction. The rhombohedral cell contains three such lamellae, corresponding to the three copies of the primitive cell in a hexagonal setting of a rhombohedral cell. In the equivalent direction of the α-phase cell (i.e., along the pseudo-monoclinic *a* axis) there are only four lamellae, but they are quite distinct, giving rise to the four-fold superstructuring observed (Fig. 3a middle). It is particularly notable that three consecutive lamellae contain interstitial Zn atoms, while the forth layer is devoid of these, and corresponds to a perfect Zn_6Sb_5-type structure. Thus we may view the α-phase as a periodic intergrowth of two phases, a hypothetical phase B, three lamellae thick, containing fully ordered interstitials, and having the composition $Zn_{40}Sb_{30}$ (Zn_4Sb_3), and a phase, A, consisting of single lamellae without any interstitial zinc of the composition $Zn_{12}Sb_{10}$ (Zn_6Sb_5). This adds up to the total composition $Zn_{52}Sb_{40}$ ($Zn_{13}Sb_{10}$). It is important to note that the lamellae description of superstructuring will equally apply along the pseudomonoclinic *c*-axis of α-Zn_4Sb_3. This observation will become crucial when arriving at an explicit structural model of α′-Zn_4Sb_3, which is presented in Section 5.

Zn deficiency in α-Zn_4Sb_3 can now be understood as missing interstitial clusters within a three-layer block

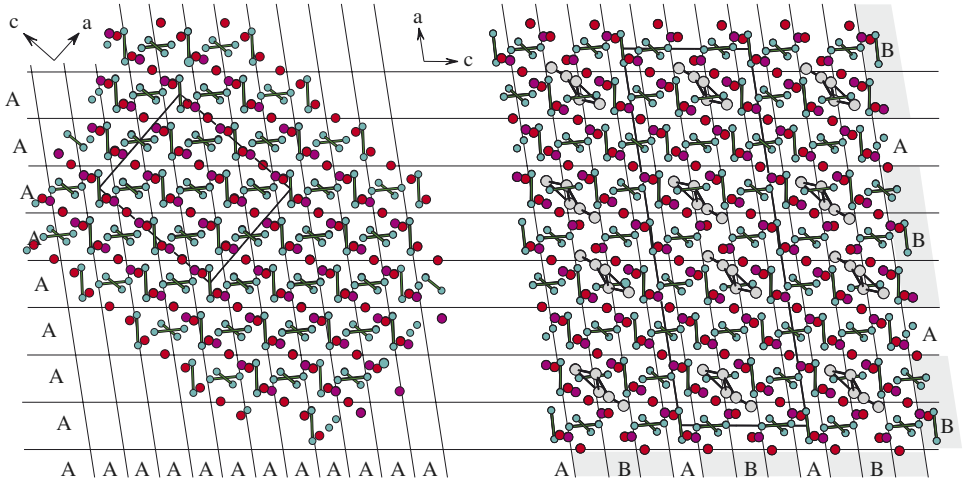

Fig. 2. The rhombohedral $Zn_{12}Sb_{10}$ framework (left) and the structure of triclinic α-Zn_4Sb_3 (right-hand side) viewed along [0 1 0]. The color code is as in Fig. 1. Bonds are drawn between short Zn contacts within interstitial clusters and rhomboid rings Zn_2Sb_2. The projection allows the comparison between the $Zn_{12}Sb_{10}$ framework and the α-Zn_4Sb_3 structure in terms of lamellae A (solid lines). In α-Zn_4Sb_3 clusters of interstitials and vacancies are confined in three consecutive lamellae (block B, composition $Zn_{40}Sb_{30}$) which are separated by an interstitial free lamella A (composition $Zn_{12}Sb_{10}$). The AB sequence yields a crystallographic composition $Zn_{52}Sb_{40}$ ($Zn_{13}Sb_{10}$) for α-Zn_4Sb_3. Note, that lamellae can be defined along the pseudo-monoclinic *a* and *c* directions of α-Zn_4Sb_3.

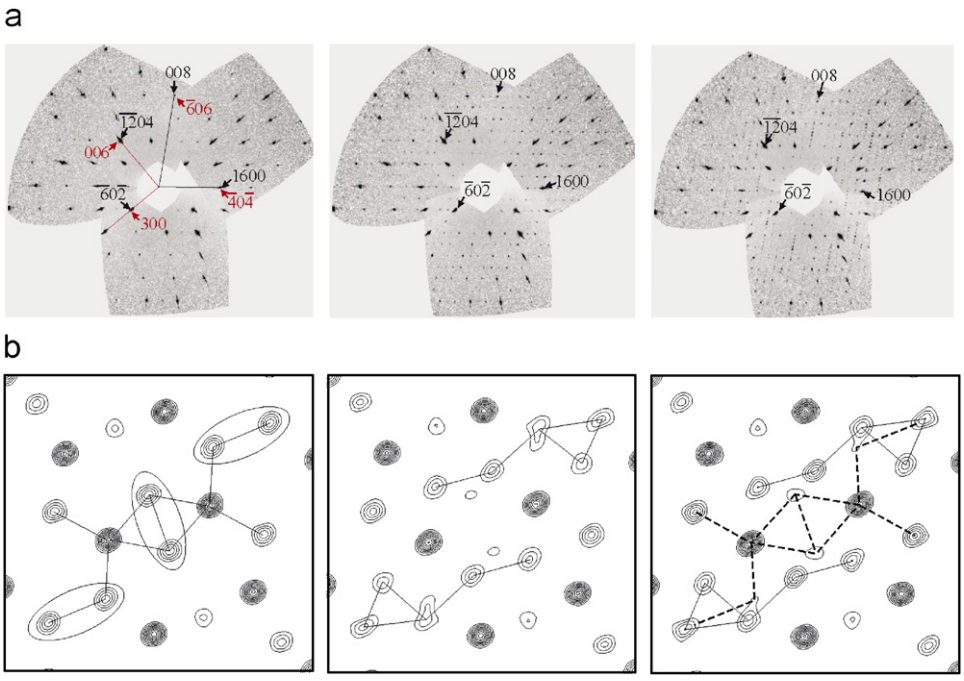

Fig. 3. X-ray diffraction patterns (a) and Fourier maps (b) for β-Zn_4Sb_3 (left), α-Zn_4Sb_3 (middle) and α'-Zn_4Sb_3 (right). Hexagonal axes and indices of rhombohedral β-Zn_4Sb_3 are shown in red ([0 1 0]* direction) and pseudo-monoclinic axes and indices of triclinic α-Zn_4Sb_3 are shown in black. The superstructure reflections of the α phase lead to a quadrupling of the $[-1\,0\,1]^*_{hex}$ direction which is the monoclinic c^* direction. The satellites of the α'-Zn_4Sb_3 structure appear very close to tripling the α-phase superstructure reflections. The Fourier maps were obtained from summation over a 2 Å layer and display a section of the structure containing a cluster of interstitials and vacancies (cf. Fig. 1c).

or/and the insertion of additional interstitial-free layers between blocks containing interstitials. Again, X-ray diffraction gives an average picture. The further step of ordering in α'-Zn_4Sb_3 is expressed in a 13-fold superstructure, which is associated with a 13 layer stacking sequence produced by Zn deficiency ordering (e.g., one additional interstitial-free lamella A is inserted per three blocks AB (= 12 lamellae) α-Zn_4Sb_3 structure). In electron density maps based on the α-Zn_4Sb_3 unit cell, the presence of the α' structure is expressed as the superposition of the α structure and the rhombohedral framework $Zn_{12}Sb_{10}$ of the β structure (Fig. 3b right). To complicate matters further, single crystal X-ray diffraction patterns collected below 230 K actually correspond to two-phase patterns, which indicates the coexistence of α and α' structured Zn_4Sb_3, presumably now with a slightly different Zn composition, $Zn_{13-\delta 1}Sb_{10}$ and $Zn_{13-\delta 2}Sb_{10}$, respectively ($\delta 1 < \delta < \delta 2$).

The complex low-temperature structural behavior of Zn_4Sb_3 is a consequence of Zn disorder in β-Zn_4Sb_3 and associated small compositional variations. These variations should affect the electronic properties of the material and are probably the origin of considerable scattering of measured resistivity and thermopower values. First we point out that property measurements on Zn_4Sb_3 were typically performed on polycrystalline samples. The high-temperature γ–β transition, which is traversed during cooling when preparing Zn_4Sb_3 from a binary mixture of the elements, produces cracks in the sample due to the difference in thermal expansion of the two phases [10,18]. Therefore only relatively small single crystals of β-Zn_4Sb_3 are obtained and those do not permit physical property measurements.

Polycrystalline (crack-containing) ingots of β-Zn_4Sb_3 have been prepared by gradient freeze, Bridgman, or simple solid state synthesis (melting and cooling) techniques [11–13,17,20,23–25]. Production of crack-free samples has been attempted by compacting powdered ingot samples by hot-pressing [10,26–28] or spark-plasma sintering (SPS) [23,29]. Also, a direct synthesis from the elements by hot-pressing has been reported [30,31]. Electronic properties vary for differently prepared samples, as exemplified in the following for the low temperature resistivity behavior (Fig. 4). The form of the resistivity curves varies within the temperature interval of the low-temperature phase transitions, from being saw-tooth shaped [17,23,28–30] to rectangular shaped [14,24,25]. Interestingly, Zn_4Sb_3 attains very similar resistivity values before and after its low-temperature phase transitions [32]. However, for samples exhibiting the saw-tooth shaped behavior it was sometimes found that the resistivity of the β phase attains higher values [23,28]. The reason for the differently shaped resistivity curves is not completely clear, but could be connected to variations in the crystallinity of the sample. However, it is now accepted that both mirror two consecutive phase transitions (β–α and α–α'). A third type of behavior has been observed with some SPS prepared samples: they reveal clearly only one transition (β–α', at

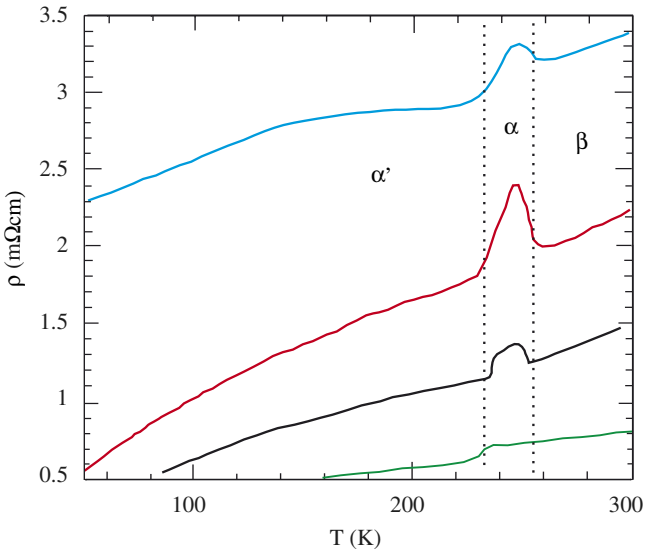

Fig. 4. Compilation of various low-temperature resistivity measurements for Zn_4Sb_3. The location of phase transitions are marked. Green: Suoma et al. [23] (SPS treated sample), black: Nylén et al. [14], Nakamoto et al. [24] (vacuum melted sample), red: Nakamoto et al. [25] (gradient-freeze prepared sample), blue: Bhattacharaya et al. [28] (sample vacuum melted, ball milled and hot pressed).

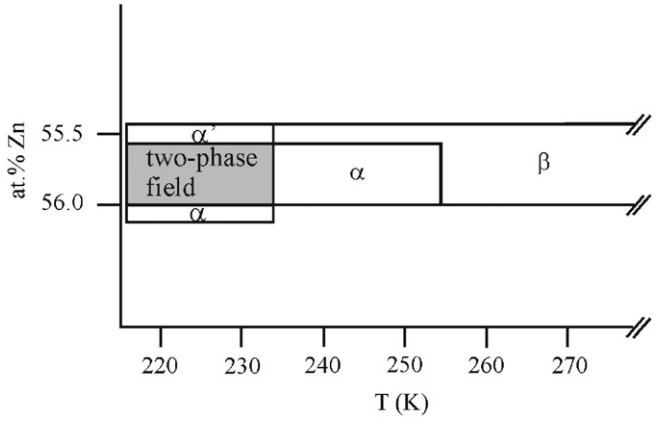

Fig. 5. Sketch of suggested phase relations for Zn_4Sb_3 at low temperatures.

around 235 K), which expresses as a small discontinuity in ρ [23,29].

The results from the structural investigations and property measurements can be brought into a consistent picture when assuming a small homogeneity range of the deficiency, $\Delta\delta = \delta 2 - \delta 1 \approx 0.3$ (0.5 at% Zn) for Zn_4Sb_3 (that is $Zn_{13-\delta}Sb_{10}$). There are two low-temperature structural transitions for Zn richer samples. For larger δ the existence of the α phase is suppressed and instead a direct transition β–α' takes place. These findings could translate into a phase diagram as sketched in Fig. 5. A slightly varying Zn content in differently prepared Zn_4Sb_3 samples can also explain the rather large scattering of measured resistivity and thermopower values for this material. Reported room temperature ρ values range from 0.8 to 3.3 mΩcm and S values from 70 to 142 μV/K [10,14,23–25,28–30].

3. Synthesis of doped samples

The typically poor crystal quality of β-Zn_4Sb_3 as obtained from direct reaction of the elements — presumably arising from traversing the γ–β phase transition — prompted us to apply the metal flux approach as an alternative synthesis. Contrary to melting and sintering methods this type of synthesis allows the preparation of intermetallics at lower temperatures and typically yields compositionally homogenous, highly crystalline, products [33]. We attempted to prepare β-Zn_4Sb_3 from zinc/antimony mixtures with ratios >1 in the presence of low melting metals Bi, Sn, In and Pb at temperatures between 520 and 670 K, which is well below the β–γ transition temperature (765 K).

For a typical reaction, a mixture of Zn, Sb and the low melting metal was pressed to a pellet and loaded into a specially prepared quartz tube which was subsequently sealed and placed in a well insulated stainless steel container. For details see Ref. [34]. The containers were heated to 923 K and kept at this temperature for 24 h to ensure complete melting and mixing of all metals. Thereafter temperature was lowered at rates between 2 and 6 K/h to a temperature between 520 and 670 K (depending on the flux composition) where the metal mixture was kept for about 2 days. Finally the obtained product was separated from the liquid excess metal mixture by centrifugation (Table 1). This procedure yielded crystals of β-Zn_4Sb_3 with sizes from one to several millimeters, which exceeds by far the size obtainable from direct reactions of the elements (Fig. 6).

When applying metal fluxes for the synthesis of Zn_4Sb_3, the third metal is unavoidably incorporated in the target material. The composition of the products was analyzed by electron microprobe analysis (EMPA) in a JEOL JXA-8600 microscope operated at 15.0 kV and 30.0 nA. Elemental metals were used as standards for Sb, Sn and Pb, while ZnS, Bi_2S_3 and InSb were used for Zn, Bi and In, respectively. The ZAF correction procedure was employed for quantitative composition determination. Additionally, the products were characterized by X-ray powder diffraction. Lattice parameters obtained from least-square refinements of the measured and indexed lines are compiled in Table 1, along with the EMPA determined compositions.

We note that the metal flux synthesis affords β-Zn_4Sb_3 with rather homogenous compositions within and between crystal specimens. The flux metal is incorporated in varying concentrations from 0.04 at% (Pb) to 1.3 at% (In). This incorporation affects the Zn/Sb ratio and produces variations far beyond the homogeneity range of the binary sample. Very low Zn concentrations are obtained with the mixtures Zn_2SbSn_5 and Zn_5Sb_2In (samples Sn-1 and In, respectively). It is noteworthy that a Pb flux does not lead to a significant incorporation of Pb. Also, the Zn

Table 1
Performed reactions and obtained products (EMPA compositions and lattice parameters from powder XRD)

Label	Starting composition	Reaction conditions	Composition [Zn, Sb, X] (at.%)	Unit cell parameters (Å)
	Zn_4Sb_3	CR 5 K/h, T 723 K, quenched	55.6(7),44.3(7)	$a = 12.234(1)$ $c = 12.429(2)$ $V = 1611.08$
Bi-1	Zn_2SbBi	T 673 K (48 h)	57.4(7), 41.5(6), 1.1(2) Bi	$a = 12.421(1)$ $c = 12.451(2)$ $V = 1615.87$
Bi-2	Zn_2SbBi_7	CR 6 K/h, T 563 K (72 h)	56.5(2), 42.9(2), 0.36(3) Bi	a = 12.2352(9) $c = 12.431(1)$ $V = 1611.62$
Sn-1	Zn_2SbSn_5	T 523 K (48 h)	54.9(4), 44.4(4), 0.66(4) Sn	$a = 12.231(1)$ $c = 12.425(1)$ $V = 1609.85$
Sn-2	Zn_5Sb_2Sn	T 723 K (48 h)	56.5(6), 43.1(5), 0.4(1) Sn	$a = 12.234(1)$ $c = 12.435(1)$ $V = 1611.86$
Pb	$ZnSbPb_5$	CR 2 K/h, T 673 K	55.8(6), 44.1(6), 0.04(8) Pb	$a = 12.226(1)$ $c = 12.419(1)$ $V = 1607.81$
In	Zn_5Sb_2In	CR 6 K/h, T 723 K	54.8(2), 43.8(1), 1.3(2) In	$a = 12.246(1)$ $c = 12.434(1)$ $V = 1614.82$

All reactions were heated to 923 K and equilibrated for 24 h. (CR = cooling rate if a ramp was applied, T = final temperature, annealing times are given in parentheses (if applied)).

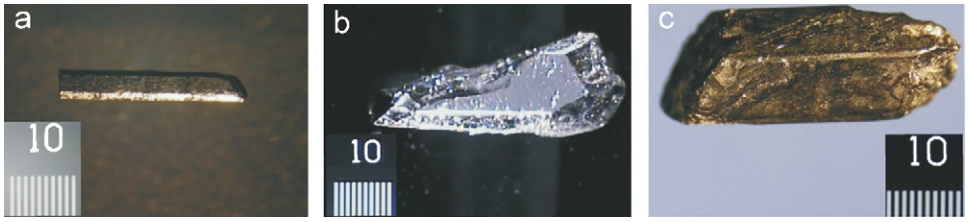

Fig. 6. Selection of β-Zn_4Sb_3 crystals obtained from molten metal flux synthesis. (a) In, (b) Sn-1, (c) Bi-1. The scale bar shows 0.1 mm separations.

concentration of the obtained product corresponds virtually to undoped β-Zn_4Sb_3. However, the Pb sample displays a different low-temperature structural behavior compared to undoped β-Zn_4Sb_3.

The case of Zn_2SbBi (sample Bi-1) is interesting in that the Zn concentration (57.4 at%) significantly exceeds that corresponding to the ideal composition of ordered α-Zn_4Sb_3 ($Zn_{13}Sb_{10}$, 56.5 at%). About 1.1 at% Bi is incorporated in Bi-1 crystals. In contrast, a reaction mixture Zn_2SbBi_7 (sample Bi-2) affords only very low Bi doping concentrations and a Zn content close to 56.5 at%. This has already been recognized by Mozharivskyj et al. [19].

Dopants can be incorporated in many ways in β-Zn_4Sb_3 (e.g., in the various substitutional or interstitial sites) and it appears difficult to establish a pattern for the obtained products. For the Bi-doped sample bismuth most likely substitutes smaller Sb, which leads to a slightly expanded crystal structure and, thus, a higher concentration of interstitial Zn can be incorporated. However, for products from Sn- and In-containing fluxes the situation is less obvious. Depending on the flux composition interstitial Zn, framework Zn, and Sb atoms may be partially substituted by the third metal. The lattice parameters and unit cell volumes of the doped samples vary only slightly (cf Table 1).

Metal fluxes offer a wide potential for the preparation of doped β-Zn_4Sb_3 in terms of temperature and flux composition. Our choices of metal mixtures, cooling rates and synthesis temperatures were performed in an exploratory manner. Crystal growth conditions can certainly be optimized by determining explicit crystallization temperatures through thermal analysis of the ternary reaction mixtures. This has not been attempted in this study. It is remarkable that (i) the reaction mixture Zn_2SbSn_5 affords β-Zn_4Sb_3 at very low temperatures (in a window 523–573 K) and that (ii) β-Zn_4Sb_3 forms from fluxes with

a large excess of Zn and a rather low concentration of the third metal, although the existence of the phase Zn_3Sb_2 in the binary Zn–Sb phase diagram would prohibit this. The Pb flux synthesis yielded crystals with a relatively small size that were only suitable for diffraction experiments. Products from reaction mixtures containing In were found to be intrinsically polycrystalline, although the crystals had clearly a single crystalline appearance (Fig. 6a). Indium doped samples of β-Zn_4Sb_3 have been previously prepared by conventional melting of Zn and Sb with small amounts of In, followed by ball milling and hot pressing. It was proposed that In substitutes Zn and that the solubility limit of In is around 3.5 at%. Higher concentrations of In in the reaction mixture led to the formation of InSb [35].

4. Low-temperature structural behavior of doped samples

4.1. Electrical resisistivity

Resistivity measurements were performed with a Quantum Design physical property measurement system (PPMS) using a four point in-line contact arrangement on rod-shaped crystals. It should be noted that mm-sized single crystals of β-Zn_4Sb_3 are unique and allow access to intrinsic resistivity thus eliminating the ambiguities of low density, cracks or grain boundaries encountered in hitherto measured polycrystalline samples. However, for this study resistivity measurements served primarily as a means for locating low-temperature phase transitions. We recall that most samples β-Zn_4Sb_3 reveal two phase transitions at 254 and 235 K to α and α'-Zn_4Sb_3, respectively, apart from presumably Zn-poor samples transforming directly to the α' phase (cf. Fig. 4).

Fig. 7a displays our findings for the Bi-doped samples Bi-1 and Bi-2. Small amounts of Bi incorporation (Bi-2) give a similar result as undoped samples when obtained as ingots from either gradient freeze or solid state methods. The $\rho(T)$ curve shows two phase transitions and no hysteresis. However, the transition temperatures are shifted slightly to lower temperatures. The consequences of higher Bi concentrations are more drastic. Upon cooling of Bi-1 (with a Bi concentration of 1.1 at% Bi) ρ decreases slightly until around 220 K where an onset to a sharp rise occurs. The resistivity takes a maximum value at about 190 K and subsequently decreases again, but then with a much higher slope. When the temperature is raised from 80 K the maximum value of ρ is reached at 215 K, after which a sharp drop occurs. The very pronounced $\rho(T)$ discontinuity between 200 and 230 K corresponds now to a single phase transition $\alpha \leftrightarrow \beta$-$Zn_4Sb_3$ (see the paragraph on diffraction experiments). Apart form the suppressed α–α' transition there are several more differences compared to the undoped sample: The β–α transition of the Bi-1 sample is shifted by about 30 K towards lower temperatures and displays a marked thermal hysteresis. The room temperature values of ρ for Bi-1 and Bi-2 are very similar to undoped β-Zn_4Sb_3 ingot samples.

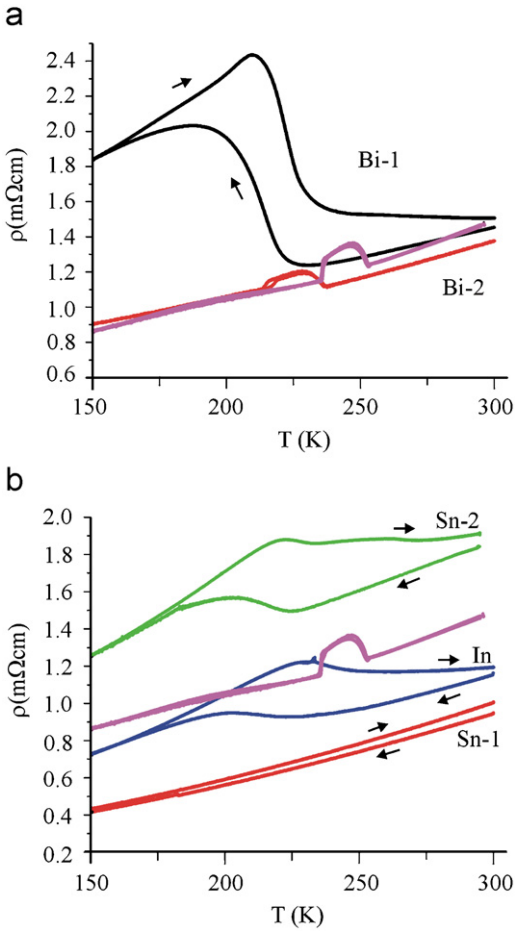

Fig. 7. Resistivity for differently doped samples Zn_4Sb_3 in comparison to the undoped material (purple). (a) Bi-1 (black) and Bi-2 (red). (b) Sn-1 (red), In (blue), and Sn-2 (green). One cooling and heating cycle are shown. Arrows indicate the direction where distinguishable.

Fig. 7b shows resistivity data for Sn-1, Sn-2 and In samples. Crystals from the Sn-2 and In samples display a similar $\rho(T)$ behaviour. The cooling curves display a bump with onset around ~220 K. This corresponds to a β–α transition and the temperature is close to the transition temperature of Bi-1 crystals. Again, the α–α' transition is suppressed (see paragraph on diffraction experiments), but the β–α transition does not appear as pronounced as for Bi-1. For Sn-1 crystals no low-temperature phase transitions occur. Even the β–α transition is suppressed.

4.2. Single crystal X-ray diffraction

Single crystal diffraction investigations of doped Zn_4Sb_3 were performed on an Oxford Diffraction Xcalibur 3 CCD diffractometer with monochromatic Mo$K\alpha$ radiation ($\lambda = 0.71073$ Å) operated at 50 kV and 40 mA and equipped with an Oxford cryo system cooler. Data collections were made at different temperatures, from 100 to 298 K with a detector distance of 50 mm. Data reduction was performed with Oxford Diffraction's CrysAlis

software [36]. Structure solutions and refinements were performed by using the program package JANA2000 [37].

We recall the structural evolution of undoped β-Zn_4Sb_3 at low temperatures: in terms of the layer description according to Fig. 2, the structure of intermediate α and low-temperature α'-Zn_4Sb_3 can be considered as four-fold and 13-fold superstructures of the rhombohedral $Zn_{12}Sb_{10}$ framework present in β-Zn_4Sb_3.

Single crystal X-ray data for Bi-1 yields the rhombohedral unit cell of β-Zn_4Sb_3 at room temperature. Cooling to 150 K gives rise to the superstructure reflections characteristic for α-Zn_4Sb_3. As a matter of fact, these reflections appear much more pronounced than for undoped Zn_4Sb_3. Further cooling to 100 K does not lead to further changes in the diffraction patterns (Fig. 8a). The electron density map of the α-phase does not indicate the structural disorder presumably arising from Zn deficiency as found for undoped α-Zn_4Sb_3 (cf. Fig. 3).

For Sn-2 single crystal data at room temperature correspond to rhombohedral β-Zn_4Sb_3. Data collection at 150 K revealed the structure of α-Zn_4Sb_3. As for Bi-1 the α'-phase is suppressed. Compared to Bi-1 and undoped β-Zn_4Sb_3, however, the diffraction patterns show a considerable amount of diffuse scattering, indicating more disorder. The electron density map (Fig. 8b) is accordingly noisy, with irregularly distributed pockets of residual electron density. In contrast single crystal data for Sn-1 collected at low temperatures did not indicate any phase transition. The room temperature β-Zn_4Sb_3 structure was preserved down to 100 K. However, diffuse scattering in the diffraction pattern indicates an initial transformation into an ordered low-temperature phase but not enough for evaluation of the crystallographic order (Fig. 8c).

An interesting case is presented by the Pb flux sample, which yielded crystals too small for resistivity measurements. We recall the peculiarity of the Pb flux not leading to any significant incorporation of Pb in β-Zn_4Sb_3 (cf. Table 1). Low-temperature diffraction experiments on Pb crystals revealed that unlike conventionally obtained, undoped, Zn_4Sb_3 the β–α transition appeared suppressed. This provided the opportunity to extract a structural model of α'-Zn_4Sb_3 from diffraction data (taken at 220 K) which are not contaminated by coexisting α-Zn_4Sb_3. In the coexisting patterns typically obtained for undoped Zn_4Sb_3 (cf. Fig. 3) basic reflections from pseudo-merohedrally twinned domains of α and α' will completely overlap for all directions (six for each phase) and for both phases [14]. In addition, the first-order satellites from the four-fold superstructure of the α phase overlap almost perfectly with the third order satellites of the 13-fold superstructure from the α' phase. Therefore, to refine the structure of the α'-phase from a mixed pattern, and even more, to solve it, appears a rather difficult task.

Proceeding now with a structure model for α'-Zn_4Sb_3 we recall that the α-phase may be regarded as an intergrowth of two hypothetical substructures, one, A, consisting of single lamellae of the composition $Zn_{12}Sb_{10}$ and a second B, consisting of triple lamellae with the composition $Zn_{40}Sb_{30}$ (Fig. 2). In terms of the substructures A and B, a simple model was constructed from the assumption that the α-phase is nothing but a plain variation of the α'-phase, in which extra A blocks have been inserted to yield a 13-fold superstructure with respect to the individual lamellae. If the α-phase is generated by the repeating sequence AB, the α'-phase is simply ABABABA.

This model was used to deconvolute the six-fold twinning of the data to yield an artificial untwinned dataset suitable for structural solution. While a fair amount of structural prejudice goes into this procedure, it should be better than simply dividing the intensities of the main reflections by six. Structural solution using charge flipping, a method known to be less susceptible to problems caused by pseudo-symmetry, was attempted on the dataset thus produced [38–40]. The principles of charge flipping are simple. A random phasing is assigned to the data, and the corresponding electron density map is calculated. Next, for all regions with electron density below a particular positive threshold, the sign of the electron density is inverted, and the resulting map is Fourier transformed to yield a new set of amplitudes and phases. The phases from this procedure are combined with the experimental amplitudes to yield a second generation model, and the process is iterated until convergence is reached. There is really only one adjustable parameter, the threshold for flipping charges. In the software (Superflip [40]) used, this threshold is set automatically to yield a certain ratio between flipped and unflipped charge. Convergence was very slow, in fact the improvement was so gradual that no convergence was detected after 10,000 cycles, but analysis of the structure solution showed that it recaptured the substructure of the β-phase and also modelled the superstructure well. Remarkably, this solution is different from the model used to deconvolute the data, and it seems more plausible in view of the details. The difference is small, but significant (Fig. 9).

As mentioned earlier, the subdivision of the underlying matrix of the $Zn_{12}Sb_{10}$ structure may be conceived in two ways, corresponding to two directions of lamella repeat. These are the directions of the pseudo-monoclinic a and c axes of the α-Zn_4Sb_3 structure. The latter allows for blocks of the A structure that are not singly lamellar but sesquilamellar in width. The α'-Zn_4Sb_3 model generated from charge flipping is best described as a stacking sequence (3/2A)BAB(3/2A)B along the c direction of α-Zn_4Sb_3 which results in an ideal composition $Zn_{84}Sb_{65}$ ($1.5\ Zn_{12}Sb_{10} + Zn_{40}Sb_{30} + Zn_{12}Sb_{10} + Zn_{40}Sb_{30} + 1.5\ Zn_{12}Sb_{10} + Zn_{40}Sb_{30} = Zn_{168}Sb_{130}$). While retaining the basic features of the original model the structure is, in fact, more homogeneous. Reverting to the original twinned data, the new structural solution was refined. Refinement is naturally not stable without special precautions being taken. All atoms of the same kind are restricted to have identical isotropic thermal displacement parameters, and the twinning must be restricted to four domains to avoid excessive

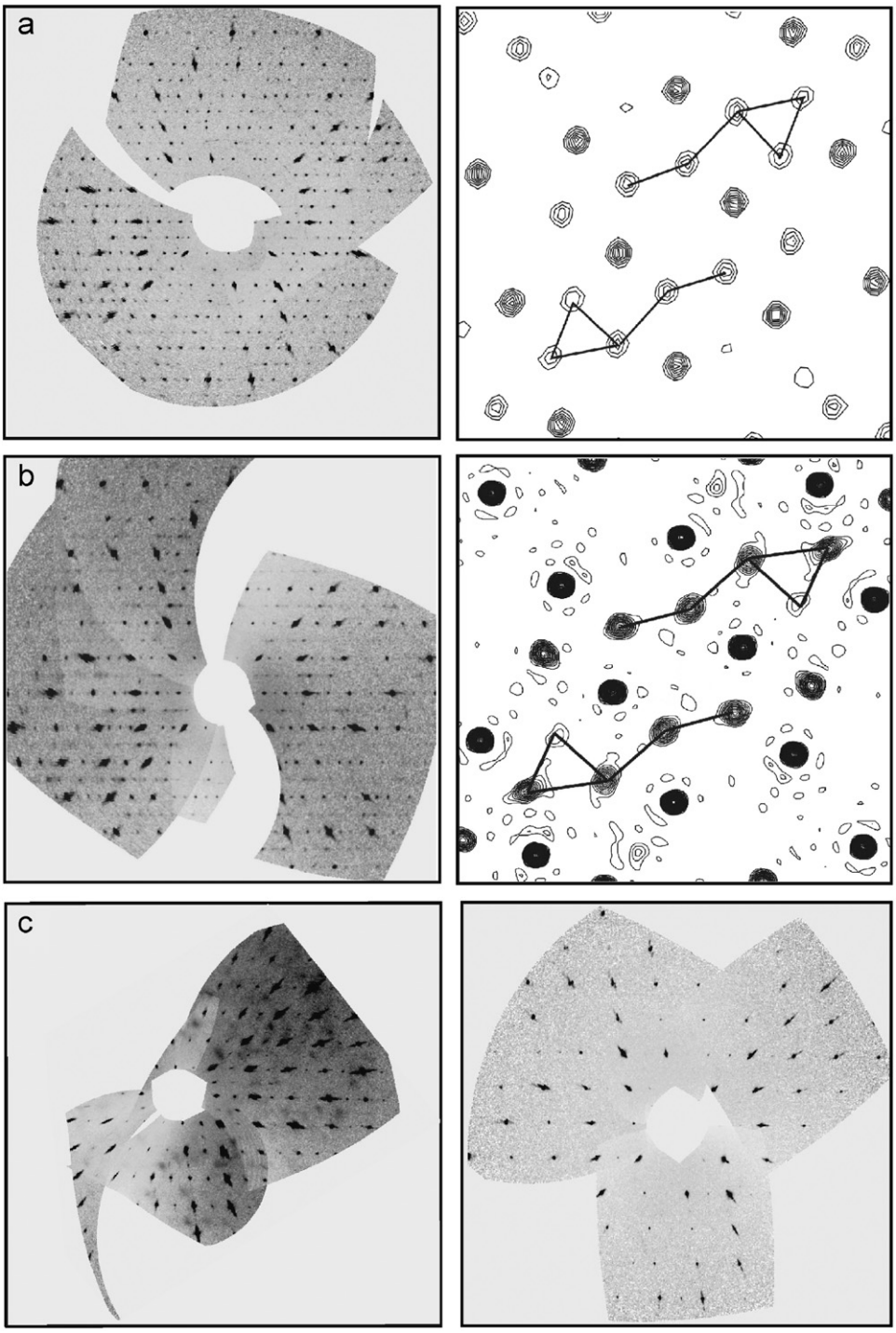

Fig. 8. X-ray diffraction patterns (left) and Fourier maps (right) for Bi-1 (a) and Sn-2 (b) at 100 and 150 K, respectively. (c) X-ray diffraction patterns of Sn-1 at 100 K (left) in comparison with that of undoped Zn_4Sb_3 at 298 K (right). All diffraction patterns are along the direction corresponding to [0 1 0]* in rhombohedral β-Zn_4Sb_3. For the Fourier maps compare with Fig. 3.

correlations. For the final model the R values are $R = 7.6$, $R_w = 8.0$ for 1754 observed reflections and 454 parameters. This is certainly much too low an observation to parameters ratio, but the result is an indication that the model is reasonable. Some details of the X-ray data collection and refinement of α'-Zn4Sb3 ($Zn_{84}Sb_{65}$) are given in Table 2 and Ref. [41].

Naturally, the insertion of an interstitial-free lamella slightly reduces the Zn composition of α'-Zn_4Sb_3 (56.4%) compared to α-Zn_4Sb_3 (56.5%). However, as for undoped Zn_4Sb_3 there is a sizeable discrepancy between the ideal crystallographic composition and the EMPA values for Pb indicating that Zn positions in α'-Zn_4Sb_3 may still be partly underoccupied.

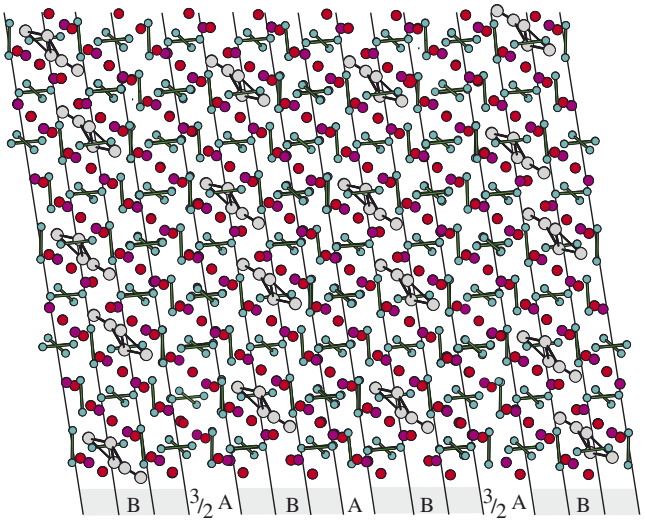

Fig. 9. The crystal structure of α′-Zn_4Sb_3 represented as stacking of interstitial-free lamellae A (composition $Zn_{12}Sb_{10}$) and interstitial containing blocks B (composition $Zn_{40}Sb_{30}$). The stacking sequence along the pseudomonoclinic c direction of α-Zn_4Sb_3 is (3/2A)BAB(3/2A)B which yields a crystallographic composition of $Zn_{84}Sb_{65}$ for α′-Zn_4Sb_3. The color code is as in Fig. 1.

Table 2
Crystallographic data of α′-Zn_4Sb_3

Empirical formula	$Zn_{84}Sb_{65}$
Formula weight	13405.7
Collection temperature	220(2) K
Radiation, wavelength (Å)	Mo $K\alpha$, 0.71073
Space group	$\bar{P}1$
a (Å)	17.3658
b (Å)	12.2319
c (Å)	106.016
α (deg)	90
β (deg)	152.0
γ (deg)	69.379
V (Å^3)	6933.322
Z	2
ρ_{calcd} (g/cm^3)	6.4193
Indep reflns	23756
$I>3\sigma(I)$, parameters	1754, 454
$R(F)$	0.076
$R_w(F)$ ($w = 1/(\sigma^2(F)+0.0001F^2)$)	0.08

Unit cell parameters could not be determined experimentally but were assessed from the 13 times superstructure relationship to the basis structure of rhombohedral β-Zn_4Sb_3.

5. Discussion

Metal doping of β-Zn_4Sb_3 has dramatic consequences for its low-temperature structural transitions. The feature of two transitions as typically observed for undoped β-Zn_4Sb_3 disappears with minute amount of a third metal incorporated (>0.1 at%). The β–α transition remains for Bi-1, In and Sn-2 samples. The latter has a rather low dopant concentration. Higher Sn concentrations appear to suppress low-temperature structural transitions completely (sample Sn-1). Compared to undoped samples, the β–α transition is shifted to lower temperature.

The composition of undoped β-Zn_4Sb_3 is $Zn_{13-\delta}Sb_{10}$, where the Zn deficiency δ is connected with a slight homogeneity range Δ. For large values of δ (~0.5) we propose that β-Zn_4Sb_3 displays only one low-temperature transition β–α′ (cf Fig. 5). It is difficult to control δ when preparing β-Zn_4Sb_3 from high-temperature synthesis of a binary mixture of Zn and Sb. According to theoretical calculations ordered α-Zn_4Sb_3 with the $Zn_{13}Sb_{10}$ (56.1 at% Zn) composition features a narrow band gap of 0.3 eV and a fully occupied valence band [22]. It is plausible to assume that the Zn deficiency relates to the metallic behavior of the resistivity of Zn_4Sb_3 and that samples with larger values of δ display a lower specific resistivity.

The consequences of metal doping to the structures of β- and α-Zn_4Sb_3 are difficult to assess. The small concentrations of the third metal component and the crystallographic problems associated with Zn disorder and structural complexity prohibits the extraction of conclusive results from X-ray diffraction experiments. In principle the dopant metal can replace Zn and Sb from regular framework sites but also replace interstitial Zn atoms and reorganize interstitial disorder considerably. Depending on the valency of the dopant metal and the kind of substitution metal doping will have consequences to electronic structure and thus electronic properties of Zn_4Sb_3.

Perhaps the easiest situation is that for Bi doping when assuming isovalent Bi substitution of Sb which would lead to a slightly expanded crystal lattice and the possibility to incorporate more interstitial Zn compared to undoped samples. As a matter of fact, the Zn content of Bi-1 is considerably higher compared to the undoped sample and actually exceeds that of the ideal composition $Zn_{13}Sb_{10}$ of α-Zn_4Sb_3. Referring to the α-phase structure it is not clear if there are disordered Zn interstitials in addition to the ordered interstitial Zn atoms or a slight substitution of Sb for Zn. Also, we cannot exclude the possibility of Zn enrichment at the surface of Bi-1 crystals or general problems associated with the EMPA measurements. Problems with determining the composition of β-Zn_4Sb_3 by EMPA have been reported in the literature [20,25]. However, our analysis is reproducible for different batches of synthesized Bi-1. The structural β–α transition is very pronouncedly expressed for Bi-1 in both resistivity and diffraction measurements. Bi-1 displays the highest resistivity for the low-temperature α modification among all samples.

The incorporation of Sn and In will affect Zn_4Sb_3 beyond size effects. Zn concentrations can drop below 55 at% (Sn-1, In) which, however, may not necessarily lead to drastically altered charge carrier concentrations when Zn is replaced by higher valent In or Sn. The room temperature resistivity values of doped samples vary between 1 and 2 mΩ cm. The lowest resistivity is observed for the Sn-1 sample with a high level of Sn doping and a

low Zn concentration. Assuming that Sn exclusively replaces interstitial Zn, Sn-1 would contain the lowest concentration of interstitial atoms among the molten metal flux prepared samples.

The low-temperature structural behavior of Zn_4Sb_3 has to be closely connected to the concentration of interstitial atoms. Based on our findings we propose the following scenario: At a high interstitial concentration (Bi-1, In, Sn-2) only a β–α transition occurs. With decreasing interstitial concentration (undoped Zn_4Sb_3) α' emerges and will gradually become the only low-temperature phase (Pb). Very low interstitial concentrations will suppress the occurrence of low-temperature structures completely (Sn-1). With molten metal flux synthesis and the accompanied incorporation of a third metal component in β-Zn_4Sb_3 much larger variations in interstitial atom concentrations are possible compared to undoped Zn_4Sb_3 where small changes arise from a tiny homogeneity range $Zn_{13-\delta}Sb_{10}$.

6. Conclusions

Molten metal flux synthesis provides an elegant route to single crystals of the structurally disordered thermoelectric material β-Zn_4Sb_3. However, the additional metal atoms are unavoidably incorporated in small concentrations (<1 at%) and act as dopants. This alters radically the subtle balance between Zn defects, Zn interstitials, and the homogeneity range δ in binary Zn_4Sb_3 ($Zn_{13-\delta}Sb_{10}$). The good thermoelectric performance of β-Zn_4Sb_3 is mainly due to its low thermal conductivity arising from structural disorder. Low-temperature structural investigations shed light on the nature of this disorder and associated compositional variations.

In this respect Zn_4Sb_3 can be put into a wider perspective: Recently it has been demonstrated that nanocrystalline inclusions embedded in bulk materials are a most effective means to reduce κ_L substantially beyond the alloy and point defect limit. In particular, very low thermal lattice conductivities (i.e., around 0.5 W/Km) can be achieved while maintaining at the same time high carrier mobilities. This is especially the case for the NaCl-type bulk thermoelectrics PbTe, which is a susceptible matrix for encapsulating a variety of different nanocrystal systems. The resulting composites (e.g., $AgPb_mSbTe_{m+2}$, $Pb_{9.6}Sb_{0.2}Te_{10-x}Se_x$) show a significantly improved thermoelectric performance compared to PbTe due to a considerably decreased κ_L [42–46].

A similar mechanism may apply to binary Zn_4Sb_3. In contrast to the specifically prepared composite systems mentioned above, nanocrystal formation in Zn_4Sb_3 occurs intrinsically as a consequence of Zn structural disorder. As a matter of fact, the actual nanocrystals are rather segregated Zn clusters in a rigid Zn–Sb framework, which only becomes apparent in low-temperature modifications of this material. Although Zn_4Sb_3 is a binary compound, the occurrence of Zn disorder makes the precise control of its composition challenging. In this respect Zn_4Sb_3 is similar to compositionally complex nanocrystal inclusion systems.

Acknowledgments

We are grateful to Lukas Palatinus for introduction to and discussions of the method of charge flipping. This work was supported by the Swedish Research Council (VR). J.N. acknowledges support from the Bengt Lundqvist and K&A Wallenberg foundations.

References

[1] (a) M.T. Tritt, M.A. Subramanian, MRS Bulletin 31 (2006) 188;
(b) G.S. Nolas, J. Poon, M.G. Kanatzidis, MRS Bulletin 31 (2006) 199.
[2] T.M. Tritt (Ed.), Recent Trends in Thermoelectric Materials Research I–III, Semiconductors and Semimetals, vols. 69–71, Academic Press, San Diego, 2000.
[3] F.J. DiSalvo, Science 285 (1999) 703.
[4] M.G. Kanatzidis, S.D. Mahanti, T.P. Hogan (Eds.), Chemistry, Physics, and Materials Science of Thermoelectric Materials, Kluver Academic/Plenum Publishers, New York, 2002.
[5] G.S. Nolas, J. Sharp, H.J. Goldsmid (Eds.), Thermoelectrics—Basic Principles and Materials Development, Springer Series in Materials Science, vol. 45, Springer, Berlin, 2001.
[6] (a) D.M. Rowe (Ed.), CRC Handbook of Thermoelectrics, CRC Press Inc., Boca Raton, FL, 1995;
(b) D.M. Rowe (Ed.), Thermoelectrics Handbook—Macro to Nano, CRC Press Inc., Florida, 2005.
[7] (a) G.D. Mahan, J. Appl. Phys. 65 (1989) 1578;
(b) J.O. Sofo, G.D. Mahan, Phys. Rev. B 49 (1994) 4565.
[8] W. Kim, J. Zide, A. Gossard, D. Klenov, S. Stemmer, A. Shakouri, A. Majumdar, Phys. Rev. Lett. 96 (2006) 045901.
[9] W. Kim, R. Wang, A. Majumdar, Nano Today 2 (2007) 40.
[10] T. Caillat, J.-P. Fleurial, A. Borshchevsky, J. Phys. Chem. Solids. 58 (1997) 1119.
[11] G.J. Snyder, M. Christensen, E. Nishibori, T. Caillat, B.B. Iversen, Nat. Mater. 3 (2004) 458.
[12] F. Cargnoni, E. Nishibori, P. Rabiller, L. Bertini, G.J. Snyder, M. Christensen, C. Gatti, B.B. Iversen, Chem. Eur. J. 10 (2004) 3861.
[13] J. Nylén, M. Andersson, S. Lidin, U. Häussermann, J. Am. Chem. Soc. 126 (2004) 1606.
[14] J. Nylén, S. Lidin, M. Andersson, B.B. Iversen, H. Liu, N. Newmann, U. Häussermann, Chem. Mater. 19 (2007) 834.
[15] Y.A. Ugai, T.A. Marshakova, V.Y. Shevchenko, N.P. Demina, Izv. Akad. Nauk SSSR, Neorg. Mater. 5 (1969) 1381.
[16] V.Y. Shevchenko, V.A. Skripkin, Y.A. Ugai, T.A. Marshakova, Izv. Akad. Nauk SSSR Neorg. Mater. 4 (1968) 1359.
[17] Y. Mozharivskyj, A.O. Pecharsky, S. Bud'ko, G.J. Miller, Chem. Mater. 16 (2004) 1580.
[18] V. Izard, M.C. Record, J.C. Tedenac, S.G. Fries, Calphad 25 (2002) 567.
[19] Y. Mozharivskyj, Y. Janssen, J.L. Harringa, A. Kracher, A.O. Tsokol, G.J. Miller, Chem. Mater. 18 (2006) 822.
[20] G. Nakamoto, N. Akai, M. Kurisu, I.-H. Kim, S.-C. Ur, V.L. Kuznetsov, J. Alloys Compd. 432 (2007) 116.
[21] H.W. Mayer, I. Mikhail, K. Schubert, J. Less-Common Met. 59 (1978) 43.
[22] A.S. Mikhaylushkin, J. Nylén, U. Häussermann, Chem. Eur. J. 11 (2005) 4912.
[23] T. Souma, G. Nakamoto, M. Kurisu, J. Alloys Compd. 340 (2002) 275.

[24] G. Nakamoto, T. Souma, M. Yamaba, M. Kurisu, J. Alloys Compd. 377 (2004) 59.
[25] G. Nakamoto, N. Akai, M. Kurisu, J. Alloys Compd. 437 (2007) 151.
[26] T.J. Zhu, X.B. Zhao, M. Yan, S.H. Hu, T. Li, B.C. Zhou, Mater. Lett. 46 (2000) 44.
[27] (a) S.-C. Ur, P. Nash, I.-H. Kim, J. Alloys Compd. 361 (2003) 84; (b) S.-C. Ur, P. Nash, I.-H. Kim, J. Mater. Sci. 38 (2003) 3553.
[28] S. Bhattacharya, R.P. Hermann, V. Keppens, T.M. Tritt, G.J. Snyder, Phys. Rev. B 74 (2006) 134108.
[29] B.L. Pedersen, H. Birkedal, B.B. Iversen, M. Nygren, P.T. Frederiksen, Appl. Phys. Lett. 89 (2006) 242108.
[30] S.-C. Ur, I.-H. Kim, P. Nash, Mater Lett. 58 (2004) 2132.
[31] I.-H. Kim, J.-B. Park, T.-W. Hong, S.-C. Ur, Y.-G. Lee, S.-L. Ryu, G. Nakamoto, M. Kurisu, Mater. Sci. Forum 510–511 (2006) 1070.
[32] A.P. Litvinchuk, B. Lorenz, F. Chen, J. Nylén, U. Häussermann, S. Lidin, L. Wang, A.M. Guloy, Appl. Phys. Lett. 90 (2007) 181920.
[33] M.G. Kanatzidis, R. Pöttgen, W. Jeitschko, Angew. Chem. Int. Ed. 44 (2005) 7023.
[34] M. Boström, S. Hovmöller, J. Solid State Chem. 153 (2000) 398.
[35] M. Tsutsui, L.T. Zhang, K. Ito, M. Yamaguchi, Intermetallics 12 (2004) 809.
[36] CrysAlis, Software for automated data collection and reduction, Oxford Diffraction, 2006.
[37] V. Petricek, M. Dusek, JANA2000, Institute of Physics, Praha, Czech Republic, 2000.
[38] G. Oszlányi, A. Sütő, Acta Crystallogr. A 60 (2004) 134.
[39] G. Oszlányi, A. Sütő, Acta Crystallogr. A 61 (2005) 147.
[40] L. Palatinus, Acta Crystallogr. A 60 (2004) 604.
[41] The CIF may be obtained from Fachinformationszentrum Karlsruhe, 76344 Eggenstein-Leopoldshafen, Germany (fax: +49 7247 808 666; email: crysdata@fiz-karlsruhe.de) on quoting the depository number CSD-418213.
[42] J. Androulakis, K.F. Hsu, R. Pcionek, H. Kong, C. Uher, J.J. DAngelo, A. Downey, T. Hogan, M.G. Kanatzidis, Adv. Mater. 18 (2006) 1170.
[43] P.F.P. Poudeu, J. D'Angelo, H.J. Kong, A. Downey, J.L. Short, R. Pcionek, T.P. Hogan, C. Uher, M.G. Kanatzidis, J. Am. Chem. Soc. 128 (2006) 14347.
[44] J.R. Scotsman, R.J. Pcionek, H.J. Kong, C. Uher, M.G. Kanatzidis, Chem. Mater. 18 (2006) 4993.
[45] H. Lin, E.S. Bozin, S.J.L. Billinge, E. Quarez, M.G. Kanatzidis, Phys. Rev. B 72 (2005) 174113.
[46] E. Quarez, K.F. Hsu, R. Pcionek, N. Frangis, E.K. Polychroniadis, M.G. Kanatzidis, J. Am. Chem. Soc. 127 (2005) 9177.